J. Fluid Mech. (1993), *vol.* 246, *pp.* 225–247

Turbulence measurements in axisymmetric jets of air and helium. Part 2. Helium jet

By N. R. PANCHAPAKESAN AND J. L. LUMLEY
Sibley School of Mechanical and Aerospace Engineering, Cornell University, Ithaca, NY 14850, USA

(Received 13 March 1991 and in revised form 29 June 1992)

A turbulent round jet of helium was studied experimentally using a composite probe consisting of an interference probe of the Way–Libby type and an ×-probe. Simultaneous measurements of two velocity components and helium mass fraction concentration were made in the x/d range 50–120. These measurements are compared with measurements in an air jet of the same momentum flux reported in Part 1. The jet discharge Froude number was 14000 and the measurement range was in the intermediate region between the non-buoyant jet region and the plume region. The measurements are consistent with earlier studies on helium jets. The mass flux of helium across the jet is within $\pm 10\%$ of the nozzle input. The mean velocity field along the axis of the jet is consistent with the scaling expressed by the effective diameter but the mean concentration decay constant exhibits a density-ratio dependence. The radial profiles of mean velocity and mean concentration agree with earlier measurements, with the half-widths indicating a turbulent Schmidt number of 0.7. Significantly higher intensities of axial velocity fluctuations are observed in comparison with the air jet, while the intensities of radial and azimuthal velocity fluctuations are virtually identical with the air jet when scaled with the half-widths. Approximate budgets for the turbulent kinetic energy, scalar variance and scalar fluxes are presented. The ratio of mechanical to scalar timescales is found to be close to 1.5 across most of the jet. Current models for triple moments involving scalar fluctuations are compared with measurements. As was observed with the velocity triple moments in Part 1, the performance of the *Full* model that includes all terms except advection was found to be very good in the fully turbulent region of the jet.

1. Introduction

Turbulent flows with density fluctuations are important both in natural and in technological processes. Density variations may be brought about by either temperature variations as in combustion or variations in composition as in mixing of gases. There is a need to understand turbulent flows of simple geometry like the axisymmetric jet with density fluctuations as a prelude to understanding and predicting more complex flows. Models for variable-density turbulent flows are now being developed in the wake of significant developments in modelling of constant-density flows. There is however very little data available to test such models. Axisymmetric jets with density fluctuations have been studied extensively though few studies provide measurements of both velocity and density fields. Second-order modelling schemes that attempt to calculate these complex flows need measurements of higher moments involving correlations of both fields. The present study in an axisymmetric jet of helium discharging into the quiescent ambient air was taken up

with these objectives in mind. The complementary study of air jet reported in Part 1 (Panchapakesan & Lumley 1993) was done at the same nozzle momentum efflux to facilitate a detailed comparison.

Complex turbulent flows are most satisfactorily modelled using second-order closure techniques. For a comprehensive survey of this subject see Lumley (1978). Models for velocity triple moments were evaluated in (I). Shih, Lumley & Janicka (1987) describe modelling techniques for variable-density flows. They performed a careful order-of-magnitude analysis in relative density fluctuations and in ratio of lengthscales and found, to first order, that constant-density models may be used for triple moments and that the effects of density variations are felt only through mean momentum and continuity equations in flows with small density fluctuations. The constant-density models for triple moments involving scalar fluctuations are evaluated in §4.3 using experimental measurements in the far field of the helium jet.

A review of non-reacting turbulent mixing flows is provided by Gouldin *et al.* (1986) which includes variable-density mixing flows. Chen & Rodi (1980) review experimental data on vertical turbulent buoyant jets, and Pitts (1986) reviews axisymmetric turbulent jet flows with global density variations. Here we consider, specifically, earlier measurements made in helium jets. Keagy & Weller (1949) in their pioneering study reported measurements in a helium jet issuing from a sharp-edged orifice, made with a sampling probe for mean concentration and a Pitot probe for mean velocity. Way & Libby (1970, 1971) developed a concentration probe following a suggestion from Corrsin (1949) and reported limited measurements in a helium jet close to the nozzle. Aihara, Koyama & Morishita (1974) reported comprehensive measurements in a high-velocity small-diameter (1 mm) jet. The measurements of Aihara *et al.*, made with a hot-wire probe similar to the Way–Libby probe and confirmed with a sampling probe, included mean and second-order quantities involving both concentration and velocity. Pitts (1986) made extensive measurements of the concentration field of axisymmetric jets in co-flows with different gas pair combinations spanning a wide range of density ratios with a laser-induced Rayleigh scattering technique. Pitts' study included measurements in a free helium jet into air and a helium jet in a co-flow of air with a small velocity ratio. The findings of the above studies will be considered in detail in §4 along with the results of the present study.

A composite probe consisting of an interference probe of the Way–Libby type as modified by Sirivat & Warhaft (1982) and an $\times$-probe was used to make simultaneous measurement of instantaneous values of helium concentration and two velocity components. The experimental set-up, calibration and data reduction of the composite probe are described in §2. The equations derived in Shih *et al.* (1987) for flows with small relative density fluctuations are briefly described in §3. These form the basis for evaluation of experimental measurements and budgets presented in §§4.1–4.4. Predictions of constant-density models for triple moments involving scalar fluctuations are compared with measurements in §4.5.

2. Experimental set-up, calibration and data reduction

The flow facility used for the present study is described in Part 1. Helium was supplied to the jet tunnel from a manifold of gas bottles. A long coil of copper tube, enabled the helium flow to equilibrate to room temperature. A cascade of pressure regulators and a needle valve was used to control the speed of the jet. The turbulence intensity at the nozzle exit was 0.2%.

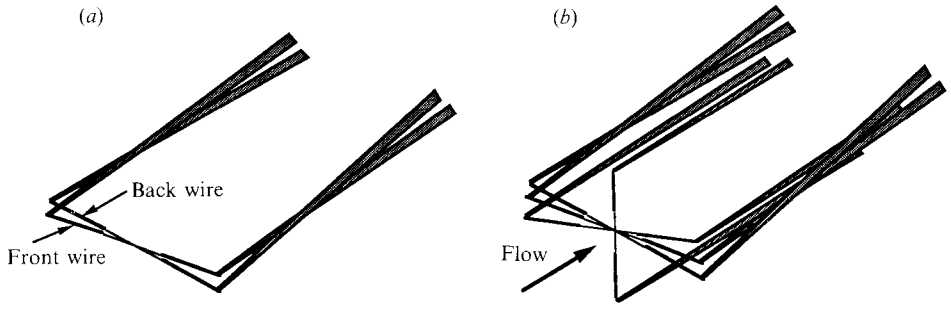

FIGURE 1. Sketch of the interference probe and the composite probe used for measurements in the helium jet. (*a*) Interference probe (Way–Libby probe) as modified by Sirivat & Warhaft (1982). (*b*) Composite probe consisting of × -probe and interference probe used for simultaneous measurement of helium concentration and two velocity components.

An interference probe of the Way–Libby type was used to measure helium concentration. The probe body of an × -wire probe (TSI 1241) was modified for use as an interference probe. We used a configuration developed by Sirivat & Warhaft (1982) and refer the reader to that work and to the original work of Way & Libby (1970) for a detailed description of the principle of operation. The probe consisted of two hot-wires, almost parallel to each other as shown in figure 1 (*a*). The hot-wire in front was a thin tungsten wire of 3 μm diameter and the back wire was 9 μm. Both wires were copper coated and the length of the central etched portion was of the order of 1 mm. The wires were soldered to the prongs. The distance between the two wires was of the order of 5 μm. The prongs that support both wires were ground as required to achieve this separation. The front wire was operated at an overheat ratio of 1.6 and the back wire at 1.8. The frequency response as determined by square-wave tests was of the order of 6 kHz. Use of lower overheat ratios for the front wire resulted in a deterioration of frequency response and was avoided. The interference probe was piggy-back mounted on an × -wire with a clamp such that the distance between the × -wire and the interference probe was the same as the separation of wires in the × -wire probe (1 mm). The resulting configuration of the composite probe is shown in figure 1 (*b*).

Helium–air mixtures for calibration were prepared in standard helium gas bottles. The partial pressures of helium and air to which the bottles were filled were determined from the desired concentration of the mixture. The mixtures were prepared ahead of time and allowed to settle for a period of one week or more. The concentration of the helium–air mixture was measured by weighing a long vertical column ($h_{\mathrm{col}} = 3.1$ m) of the mixture with the help of a differential pressure transducer. The pressure differential was measured immediately after filling the column before the mixture had any time to diffuse out.

The composite probe was calibrated in a small calibration wind tunnel of 4 in. diameter with a nozzle jet of diameter of 15 mm. The calibration was carried out over a domain determined by ranges of yaw angles, velocity and concentration. The yaw angle range was always $\pm 42°$ dictated by the × -wire probe used. The velocity range and concentration range were determined by trial runs in the jet and were dependent on the radial location in the jet at which the measurements were being carried out. Typically 15 yaw angle positions, 12 velocities and 5 concentration levels were used. The maximum concentration of the calibration gas mixture that was required for measurements on the centreline was about 0.06 (mass fraction) and the velocity range was 0.8 to 14 m/s.

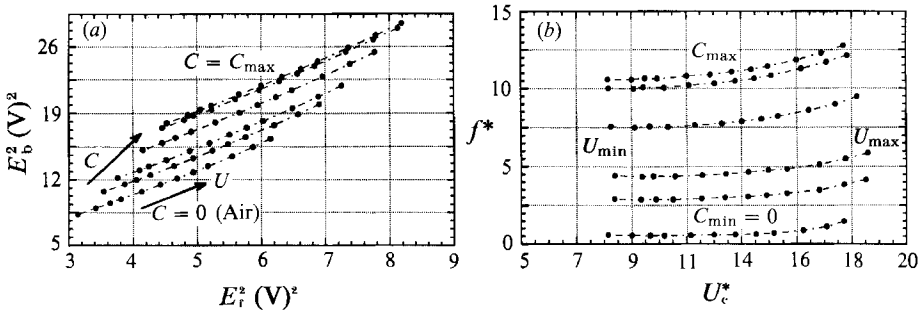

FIGURE 2. Interference probe calibration at zero yaw angle. (*a*) Plot of the front and back wire voltages for different concentrations of helium as functions of velocity. (*b*) The same data as in (*a*) after two transformations consisting of linear changes of coordinates and shear.

The basic scheme used to determine the velocity, yaw angle and concentration, U, Θ and f, from the probe voltages was the table look-up scheme described in Lueptow, Breuer & Haritonidis (1988) for an $\times$-wire probe. A modified version that was used with an $\times$-wire probe in an air jet is described in detail in Part 1. This scheme was treated as a device to effect a co-ordinate change in a two-dimensional domain and was used for the concentration probe voltages also. For this scheme to be effective it was necessary to use an initial transformation that converted the calibration domain into an almost rectangular region. For the $\times$-wire probe, the voltages (E_1, E_2) of the two wires were converted to intermediate variables $(U_\times^*\ \Theta^*)$ using King's law and the Cosine law and the table look-up scheme was used to convert $(U_\times^*, \Theta^*)$ to $(U_\times, \Theta)$ where the subscript $\times$ denotes velocities determined from the $\times$-wire probe. This procedure was applied to the calibration voltages of the $\times$-wire probe for each concentration of the helium–air mixture used.

The calibration domain for the concentration probe in (E_f^2, E_b^2) with zero yaw angle is shown in figure 2(*a*). Two successive transformations, a linear change of coordinates followed by a shear transformation, were applied to get the desired almost rectangular domain shown in figure 2(*b*). These transformations were defined completely by the calibration voltages of the concentration probe at zero yaw angle. For each yaw angle, the concentration probe voltages (E_f^2, E_b^2) were transformed to a pair of intermediate variables (U_c^*, f^*) with these transformations and the necessary coefficients that convert (U_c^*, f^*) to (U_c, f) using the same table look-up scheme were calculated and stored. The subscripts f and b indicate the front and back wires of the concentration probe and the subscript c is used to denote velocities determined from the concentration probe.

During measurement the wire voltages from the two probes (E_f, E_b) and (E_1, E_2) were converted to U, Θ and f as follows:

(i) Assume $\Theta = 0$.

(ii) Evaluate (U_c, f) from (E_f, E_b) for a given Θ.

(iii) Given f, calculate $(U_\times, \Theta)$ from (E_1, E_2) using linear interpolation between values of $(U_\times, \Theta)$ at f_i and f_{i+1} where $f_i \leqslant f \leqslant f_{i+1}$.

(iv) Repeat steps (ii) and (iii) with updated value of Θ if Θ calculated in step (iii) is different from Θ assumed in step (ii).

Of the two velocities $U_\times$ and U_c, the velocity $U_\times$ from the $\times$-wire probe was the one used in calculation of all moments. Differences between $U_\times$ and U_c during measurement were very small and were within the range expected from the spatial separation and the difference in the frequency responses of the two probes. The r.m.s.

errors for the conversion of the $\times$-probe voltages (E_1, E_2) to $(U_\times, \Theta)$ at a particular mixture concentration were 1.0 cm/s and 0.5°. The values for the interference probe for conversion of (E_f, E_b) to (U_c, f) at a particular yaw angle were 2.0 cm/s and 10^{-4} for U and C for the range of variables indicated earlier.

The composite probe was moved with a shuttle through the jet as described in Part 1. At each radial location the probe was mounted in two perpendicular orientations to measure (u, v, f) and (u, w, f). The averages of moments other than the mean were obtained with 1000 traverses of the shuttle which took about 3 h. The mean velocity and mean concentration fields were obtained with measurements done on a single day with averages of 100 traverses of the shuttle. This was done to avoid calibrating the probe too often; mean fields were found to be affected by the calibration drifts associated with temperature changes. As a consequence of this small statistical sample the mean fields in figures 3 and 4 are not very smooth. The ambient temperature changes from day to day were found to affect the mean quantities slightly but not the higher moments and a simple correction scheme was not feasible for the composite probe. During each measurement the calibration of the probe was partially checked with traverses of the shuttle in quiescent air.

3. Governing equations

We use the coordinate system and notation defined in Part 1. In addition we use ρ, ρ' and ρ'' to denote density, fluctuation of density and the r.m.s. value of density fluctuations respectively. The average density is denoted as $\langle\rho\rangle$. Mean mass fraction of helium and its fluctuation are denoted by F and f. A tilde indicates the instantaneous total value of that quantity.

The relation between the density and the mass fraction is given by

$$\tilde{\rho} = 1/(c\tilde{f}+e), \tag{1}$$

$$c = (1/\rho_h)-(1/\rho_a), \quad e = 1/\rho_a, \tag{2}$$

where the subscripts h and a denote helium and air respectively. The conservation equations for the instantaneous quantities of mass fraction and momentum and the continuity equation are

$$\tilde{f}_{,t}+\tilde{u}_k\tilde{f}_{,k} = (1/\tilde{\rho})(\gamma\tilde{\rho}\tilde{f}_{,k})_{,k}, \tag{3}$$

$$\tilde{u}_{i,t}+\tilde{u}^j\tilde{u}_{i,j} = -(1/\tilde{\rho})[\tilde{\rho}+\tfrac{2}{3}\mu\tilde{u}^p_{,p}]_{,i}+\nu g^{kj}(\tilde{u}_{i,j}+\tilde{u}_{j,i})_{,k}+g_i, \tag{4}$$

$$\tilde{\rho}_{,t}+(\tilde{\rho}\tilde{u}^k)_{,k} = 0, \tag{5}$$

where γ is the molecular diffusivity of the scalar and μ is the viscosity.

Basic equations for variable-density flows in which the density fluctuations are brought about by the mixing of two gases may be derived from the above equations and are developed in detail in SLJ. They have derived equations for flows with small density fluctuations, i.e. $\rho''/\langle\rho\rangle \ll 1$. Measurements indicate that the intensity of density fluctuations in the helium jet, for $x/d > 50$, was less than 3%. With further assumptions of high turbulent Reynolds number and high Schmidt number the final equations are

mean momentum equation

$$U^jU_{i,j}+\langle u_iu^j\rangle_{,j}+\langle u_iu^j\rangle\langle\rho\rangle_{,j}/\langle\rho\rangle = -(1/\langle\rho\rangle)P_{,i}+g_i$$
$$+c\langle\rho\rangle[-\frac{1}{\langle\rho\rangle}\langle p_{,i}f\rangle-(\nu+\gamma)g^{jk}\langle u_{i,k}f_{,j}\rangle-\langle u_iu^j\rangle F_{,j}]. \tag{6}$$

mean mass fraction equation

$$U^j F_{,j} + \langle fu^j \rangle_{,j} + \langle fu^j \rangle \langle \rho \rangle_{,j} / \langle \rho \rangle = c \langle \rho \rangle [-2 \langle \epsilon_f \rangle - \langle fu^j \rangle F_{,j}]. \tag{7}$$

scalar variance equation

$$U^j \langle f^2 \rangle_{,j} + 2 \langle fu^j \rangle F_{,j} + \{ \langle f^2 u^j \rangle_{,j} + \langle f^2 u^j \rangle \langle \rho \rangle_{,j} / \langle \rho \rangle \} = -2\epsilon_f + c \langle \rho \rangle [- \langle f^2 u^j \rangle F_{,j} - 4\gamma g^{km} \langle ff_{,k} f_{,m} \rangle]. \tag{8}$$

scalar flux equation

$$\begin{aligned} U^j \langle fu_i \rangle_{,j} + \{ \langle fu^j \rangle U_{i,j} + \langle u_i u^j \rangle F_{,j} \} + \{ \langle fu_i u^j \rangle_{,j} + \langle fu_i u^j \rangle \langle \rho \rangle_{,j} / \langle \rho \rangle \} \\ = - \langle p_{,i} f \rangle / \langle \rho \rangle - (\nu + \gamma) g^{kj} \langle f_{,k} u_{i,j} \rangle \\ + c \langle \rho \rangle [- (P_{,i} / \langle \rho \rangle) \langle f^2 \rangle - \langle p_{,i} f^2 \rangle / \langle \rho \rangle - \langle fu_i u^j \rangle F_{,j}]. \end{aligned} \tag{9a}$$

or, alternatively

$$\begin{aligned} U^j \langle fu_i \rangle_{,j} + \{ \langle fu^j \rangle U_{i,j} + \langle u_i u^j \rangle F_{,j} \} + (1/\langle \rho \rangle) (\langle \rho \rangle \langle fu_i u^j \rangle)_{,j} \\ = - \langle p_{,i} f \rangle / \langle \rho \rangle - (\nu + \gamma) g^{kj} \langle f_{,k} u_{i,j} \rangle \\ + c \langle \rho \rangle [- P_{,i} / \langle \rho \rangle \langle f^2 \rangle - \langle p_{,i} f^2 \rangle / \langle \rho \rangle - \langle fu_i u^j \rangle F_{,j}]. \end{aligned} \tag{9b}$$

Reynolds stress equation

$$\begin{aligned} U^m \langle u_i u^j \rangle_{,m} + \{ \langle u_i u^m \rangle U^j_{,m} + \langle u^m u^j \rangle U_{i,m} \} + \{ \langle u_i u^j u^m \rangle_{,m} + \langle u_i u^j u^m \rangle \langle \rho \rangle_{,m} / \langle \rho \rangle \} \\ = - \frac{1}{\langle \rho \rangle} (\langle p_{,i} u^j \rangle + g^{kj} \langle p_{,k} u_i \rangle) - 2\nu g^{km} \langle u_{i,m} u^j \rangle \\ + c \langle \rho \rangle [- (1/\langle \rho \rangle) (P_{,i} \langle fu^j \rangle + P_{,k} \langle fu_i \rangle g^{kj}) \\ - (1/\langle \rho \rangle) (\langle p_{,i} fu^j \rangle + \langle p_{,k} fu_i \rangle g^{kj}) - \langle fu^k \rangle \langle u_i u^j \rangle_{,k} \\ - \langle u_i u^j u_k \rangle F_{,k}], \end{aligned} \tag{10a}$$

or alternatively

$$\begin{aligned} U^m \langle u_i u^j \rangle_{,m} + \{ \langle u_i u^m \rangle U^j_{,m} + \langle u^m u^j \rangle U_{i,m} \} + (1/\langle \rho \rangle) (\langle \rho \rangle \langle u_i u^j u^m \rangle)_{,m} \\ = - (1/\langle \rho \rangle) (\langle p_{,i} u^j \rangle + g^{kj} \langle p_{,k} u_i \rangle) - 2\nu g^{km} \langle u_{i,m} u^j_{,k} \rangle \\ + c \langle \rho \rangle [- (1/\langle \rho \rangle) (P_{,i} \langle fu^j \rangle + P_{,k} \langle fu_i \rangle g^{kj}) \\ - (1/\langle \rho \rangle) (\langle p_{,i} fu^j \rangle + \langle p_{,k} fu_i \rangle g^{kj}) - \langle u_i u^j u^k \rangle F_{,k}] \end{aligned} \tag{10b}$$

In the above equations (from (8) on) the three terms on the left-hand side respectively represent advection, production and diffusion; the first two terms on the right-hand side represent pressure and dissipation (there is no pressure term in (8)); and the effects of variable density are represented by terms preceded by the factor $c\langle \rho \rangle$. We will present budgets for the turbulent kinetic energy, scalar variance and scalar fluxes in §4.3 based on the above equations.

4. Results

4.1. *Mean quantities*

Variation of the axial mean velocity along the centreline plotted as U_j/U_s *vs.* x/d is shown in figure 3. The experimental data shown, as explained earlier, are the average of 100 traverses of the shuttle. The nonlinear polynomial curve fit to the experimental data and the best linear fit through $x/d = 0$ are also shown. The linear fit to the data is given by $U_j/U_s = 0.414\ x/d$. The decay constant of 0.414 compares favourably with the value of 0.444, estimated from the air jet measurements reported in Part 1

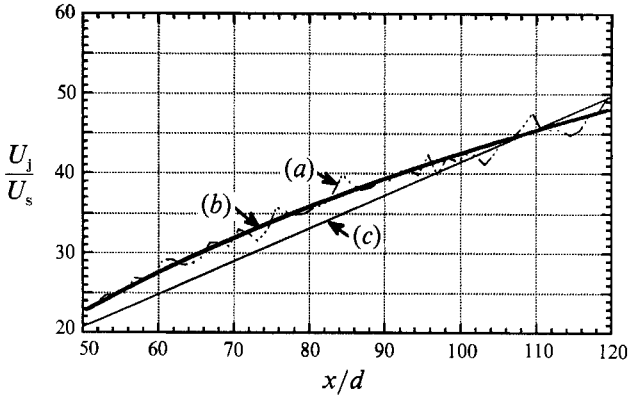

FIGURE 3. Variation of the axial mean velocity U_s along the jet centreline. U_j is the jet nozzle velocity. (*a*) Average of 100 traverses of the shuttle. (*b*) Nonlinear polynomial curve fit. (*c*) Linear fit to the data through the point $x/d = 0$ given by $U_j/U_s = 0.414\ x/d$.

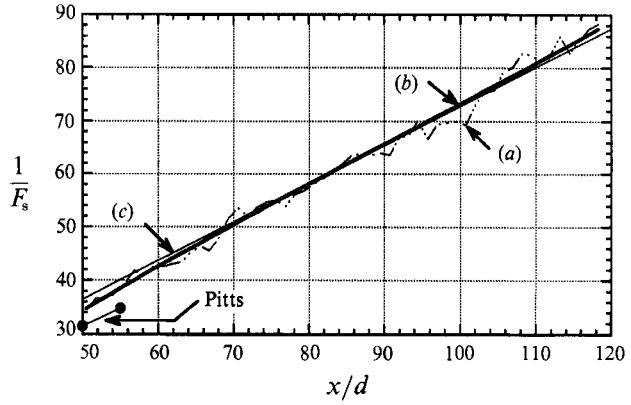

FIGURE 4. Variation of the mean helium concentration F_s measured in mass fraction units along the jet centreline. See figure 3 for explanation of the symbols. The linear fit to the data is given by $1/F_s = 0.73\,x/d$. Data from Pitts (1986) are also shown.

using the concept of effective diameter defined as $d_e = \omega^{-\frac{1}{2}} d$, where $\omega = \rho_a/\rho_h = 7.24$. The reciprocal of the centreline mass fraction is plotted as a function of x/d in figure 4. The nonlinear polynomial curve fit to the data is not very different from the least-squares linear fit through the origin $x/d = 0$. The linear fit is given by $1/f_m = 0.73\ x/d$. If the data are represented in the form $1/f_m = K_c\, x/d_e$, the value of K_c is found to be 0.271. Pitts (1986) finds K_c to be 0.256 for his measurement in a free helium jet with laser-induced Rayleigh scattering and also quotes a value of 0.214 for the measurement of Keagy & Weller. Both these values are for x measured from a virtual origin x_0, while the present value uses the distance from the nozzle.

In order to compare the present measurements with data taken in other vertical turbulent jets using fluids of different density ratios we consider the non-dimensionalization advocated by Chen & Rodi (1980) which facilitates a unified representation of the experimental data (see also Ogino *et al.* 1980).

The parameters that govern the global development of a vertical turbulent buoyant jet are the initial momentum flux M_j, the weight deficit W_j and the ambient air density ρ_a:

$$M_j = \rho_j U_j^2 d^2, \tag{11}$$

$$W_j = g(\rho_a - \rho_j)\, U_j\, d^2. \tag{12}$$

The subscript j indicates conditions at the nozzle, and $\rho_j = \rho_h$. The factor $\frac{1}{4}\pi$ in the nozzle area has been omitted to conform to Chen & Rodi. The following non-dimensional quantities for length, velocity and buoyant force can be defined with the help of dimensional analysis:

$$x_1 = F^{-\frac{1}{2}}\omega^{\frac{1}{4}}(x/d), \quad U_1 = F^{\frac{1}{2}}\omega^{\frac{1}{4}}(U/U_j) \quad g_1 = F^{\frac{1}{2}}\omega^{-\frac{3}{4}}C^*, \tag{13a–c}$$

where $$C^* = (\rho_a - \langle\rho\rangle)/(\rho_a - \rho_j), \quad F = U_j^2\rho_j/(\rho_a - \rho_j)\,gd$$

are the dimensionless density and densimetric Froude number respectively.

The flow field can be divided into three regions according to the relative importance of buoyancy: non-buoyant jet region (NBJ), the intermediate region (I) and the buoyant plume region (BP). The limiting regions, NBJ and BP, admit self similar-solutions to the equations of motion when ω is of order 1. The similarity solution is only approximate in the NBJ region when there are strong density fluctuations. For the helium jet $\omega = 7.24$, hence deviations from the self-similar decay patterns should be expected. The decay laws for velocity and concentration along the axis of the jet in the two limiting regions are given by

$$\text{NBJ:} \quad U_1 = A_u\omega^{\frac{1}{2}}x_1^{-1}, \quad g_1 = A_\rho\omega^{-\frac{1}{2}}x_1^{-1}, \tag{14a}$$

$$\text{BP:} \quad U_1 = B_u\omega^{\frac{1}{3}}x_1^{-\frac{1}{3}}, \quad g_1 = B_\rho\omega^{-\frac{1}{3}}x_1^{-\frac{5}{3}}. \tag{14b}$$

The factors A_u, A_ρ, B_u and B_ρ need to be determined from experiments. Since the above relationships should be independent of the density ratio ω, these factors can be determined from experiments done with $\omega = 1 : A_{u1} = A_u\omega^{\frac{1}{2}}$ etc. The relationships given above for the non-buoyant jet are consistent with the effective-diameter concept introduced by Thring & Newby (1953). Chen & Rodi (1980), after reviewing existing experimental data, chose

$$A_{u1} = 6.2, \quad A_{\rho 1} = 5.0. \quad B_{u1} = 3.5, \quad B_{\rho 1} = 9.35. \tag{15}$$

They identified points $x_1 = 0.5$ and $x_1 = 5$ to delineate the three regions after considering the experimental data. Ogino *et al.* chose 1 and 5 after extensive measurements in water jets with different discharge Froude numbers spanning all three regions. A lengthscale similar to the Monin–Oboukhov scale that indicates when the buoyant forces become significant can be defined from the volume flux and the buoyancy flux at the nozzle (see e.g. Papanicolaou & List 1987), which for the present flow is given by $L_M/d = 110$ ($x_1 = 1.5$). Pitts (1986) derived a formula for the mean momentum added by the buoyancy as a function of the axial distance by assuming hyperbolic decay of mean concentration along the axis and a self-similar profile for the radial variation. These assumptions are found to be approximately valid for the present flow and calculations according to Pitts' formula indicate that the ratio of buoyancy added momentum to the nozzle momentum efflux is given by $0.15x_1^2$ and the two would be of the same order at $x/d = 190$, i.e. $x_1 = 2.6$. Thus the range of x/d over which measurements have been made in the present study may be considered to lie in the intermediate region between the non-buoyant region and the plume region.

Flow parameters for earlier studies of the helium jet are given in table 1, together with the data for the present study. The x_1 values for all the studies have been calculated from the published jet exit conditions and these are also shown in table 1. Distances are measured from the nozzle exit and no corrections for virtual origins have been made. The measurements of Keagy & Weller and Aihara *et al.* are completely in the non-buoyant region, while the present study and that of Way & Libby fall in the intermediate region. The concentration field measurements of Pitts span both the non-buoyant region and the intermediate region. Since the nozzle exit

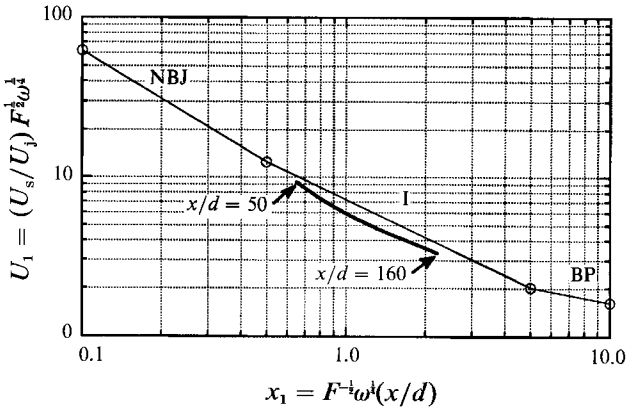

FIGURE 5. Variation of the axial mean velocity in the non-dimensional coordinates suggested by Chen & Rodi (1980) (see (13)). NBJ – non-buoyant jet region, I – intermediate region, BP – buoyant plume region. The open circles indicate the delineated points.

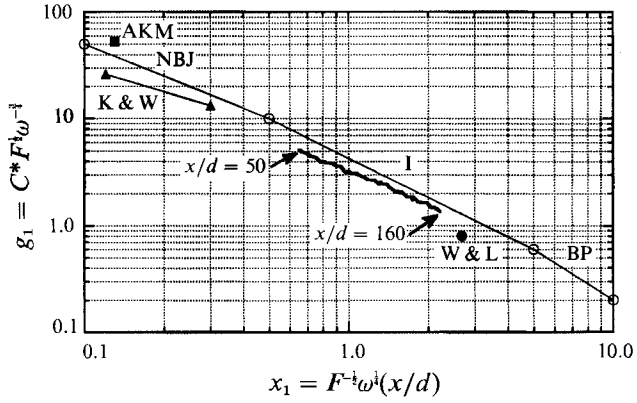

FIGURE 6. Variation of the mean helium concentration in the non-dimensional coordinates. See figure 5 for explanation. AKM – Aihara *et al.* (1974) $x/d = 100$; K & W–Keagy & Weller (1949), $x/d = 20$–50; W & L–Way & Libby (1971).

	U_j (m/s)	d (mm)	F	x/d (min)	x/d (max)	x_1 (min)	x_1 (max)
Keagy & Weller (1949)	122	3.25	7.5×10^4	10	50	0.06	0.3
Aihara *et al.* (1974)	310	1.0	1.6×10^6	30	100	0.04	0.13
Way & Libby (1971)	15.25	25.4	150	15	20	2.0	2.68
Pitts (1986)	73.25	6.35	1.4×10^4	10	55	0.14	0.76
Present	72.5	6.12	1.4×10^4	50	120	0.69	1.66

TABLE 1. Flow paramcters for various studies of the helium jet

conditions for the present study and those of Pitts are very close to each other, direct comparisons are valid.

The centreline variation of axial mean velocity and mean helium concentration are plotted in terms of these non-dimensional variables in figures 5 and 6. The linear interpolation in the intermediate region is used only as a guide; the experimental data reviewed by Chen & Rodi (1980) including those of Ogino *et al.* (1980) do make a smooth transition between the two limiting regions. The plot of the velocity data

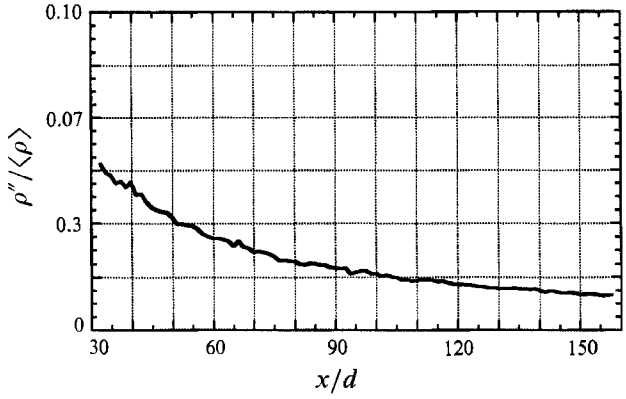

FIGURE 7. Intensity of density fluctuations along the axis of the jet; ρ'' is the r.m.s. value of density fluctuations.

shown in figure 5 is in excellent agreement with similar plots in Rodi (1982) and Ogino *et al.* and clearly indicate the approach to the expected decay rates in the two limiting regions. The plot for concentration decay is shown in figure 6. While the data approach the buoyant plume side correctly, they do not seem to do so on the non-buoyant jet side. The choice of the value of 5.0 for $A_{\rho 1}$ by Chen & Rodi, which is equivalent to $K_c = 0.2$, is primarily based on flows with ω close to 1. The current value of $K_c = 0.272$ is significantly different and reflects the effect of the large value of the density ratio ω and the consequent large density gradients in the near field. Pitts (1986) in his extensive study on effects of global density differences found a similar influence of ω on the centreline concentration decay rates. He found the factor of $\omega^{\frac{1}{2}}$ to be inadequate to correlate the results from his measurements with different density ratios and found better correlation using $\omega^{0.6}$. The agreement between the values of K_c found in these two studies of helium jets (0.272 and 0.256) supports this observation. Some representative data points from the studies of Aihara *et al.*, Keagy & Weller and Way & Libby are also shown in figure 6.

In the intermediate region the helium jet is not self-similar. In order to facilitate comparisons with other measurements made in the non-buoyant jet region and with model calculations we treat the jet as approximately self-similar in the x/d range of 90–120. In this range the mean density is very close to ambient air density. Furthermore the linear approximations to mean velocity and concentration shown in figures 3 and 4 represent the measurements very well in this region. The values predicted by these linear fits for U_s and F_s were the values used for normalization for all radial plots. The curve fits in all radial plots were based on data in the x/d range 90 to 120 and were found to be unaffected by the kind of normalization used. In contrast, for all plots that describe axial variations the values from the nonlinear polynomial fits were used as normalization factors. In the x/d range 50–80, where the differences between nonlinear and linear approximations to the mean velocity data in figure 3 are larger, some differences between radial and axial plots will be observed.

The intensity of density fluctuations along the axis and the mean density field across the jet are shown in figures 7 and 8. The very small values of the observed density fluctuations justify the use of the approximations made in deriving the equations. The mean density field shown in figure 8 compares very well with values obtained from the approximation:

$$\langle\rho\rangle = 1/(cF+e). \tag{16}$$

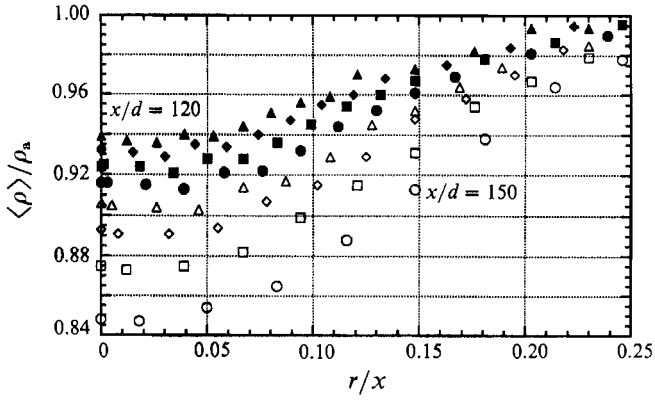

FIGURE 8. Variation of the mean density across the jet for axial locations from $x/d = 50$ *to* 120. ○, $x/d = 50$; □, 60; ◇, 70; △, 80; ●, 90, ■, 100, ◆, 110; ▲, 120.

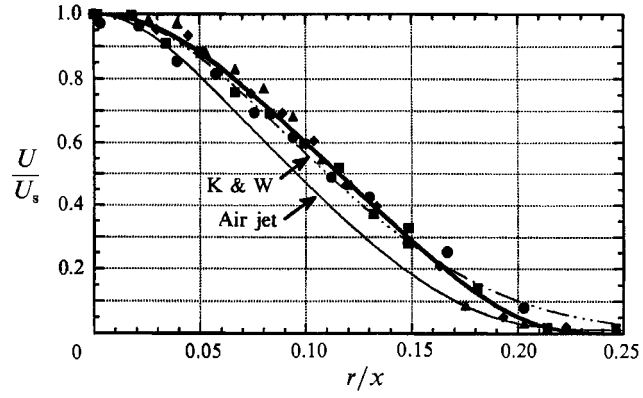

FIGURE 9. Radial profile of axial mean velocity: x/d range 90–120. See figure 8 for explanation of symbols. K & W–Keagy & Weller (1949).

All measured correlations are reported in terms of the mass fraction fluctuations. Since the density fluctuation intensities are very small they may be converted to correlations with density fluctuations with the help of the relation:

$$\rho' = c\langle\rho\rangle^2 f \tag{17}$$

as indicated in Shih *et al.* (1987).

Radial profiles of axial mean velocity and helium concentration are shown in figures 9 and 10. The velocity profile has a value of 0.5 at $\eta = 0.116$. This half-width compares very well with the value of 0.110 obtained by Keagy & Weller from measurements in the x/d range 16–24. The half-width is larger than the 0.096 observed in the air jet. Aihara *et al.* report mean velocity measurements which are significantly different from zero in the range $0.2 < \eta < 0.3$. This is not observed in the present measurements. The half-width for the profile of concentration of helium in mass fraction units shown in figure 10 is 0.138. Keagy & Weller report a value of 0.156 for the half-width of mole fraction profile. The nonlinear relation between the two concentration measures makes a direct comparison invalid, but for our purposes we may obtain an approximate value by assuming that turbulent intensities are small and that local linearization may be used. This implies that the relationship between the two measures may be applied to the averages, and yields an equivalent

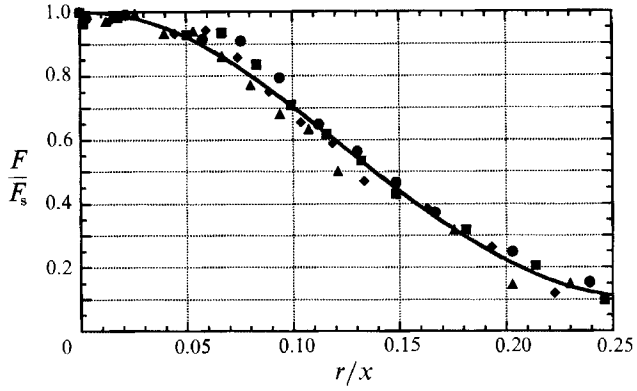

FIGURE 10. Radial profile of mean helium concentration. See figure 8 for explanation of symbols.

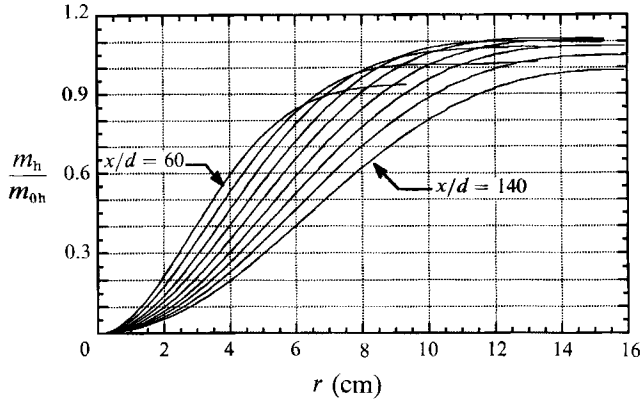

FIGURE 11. Conservation of helium mass flux–mass flux of helium across the jet normalized by the nozzle flux is plotted as a function of the radial coordinate. Only the mean field contribution has been included.

mass fraction half-width of about 0.132 for Keagy & Weller's data, which is close to the present value. Estimation of turbulent Schmidt number from the half-widths of the velocity and concentration profiles yields 0.7, which is the same as the value recommended for round jets by Chen & Rodi.

Conservation of helium mass flux is assessed by integrating the product of mean density, velocity and mass fraction across the jet at different axial locations and this value is shown as a fraction of the mass flux at the nozzle in figure 11. Turbulent contributions have not been included. The helium mass flux is seen to be conserved to within $\pm 10\%$.

4.2. *Second moments*

The turbulent intensities of axial and radial velocity fluctuations along the axis of the jet are shown in figure 12. The intensity of axial velocity fluctuations are almost twice as large as the radial and azimuthal components, a finding which has also been reported by Aihara *et al.* u'/U_s decreases from 40% at $x/d = 50$ to 34% at $x/d = 120$, while v'/U_s is between 21 and 19% in the same x/d range. In comparison with the values measured in the air jet, the axial velocity fluctuations are about 80 to 90% larger while the radial intensities are of about the same order. Tombach's measurements of u', reported in Way & Libby, in the x/d range 15–20 are about what

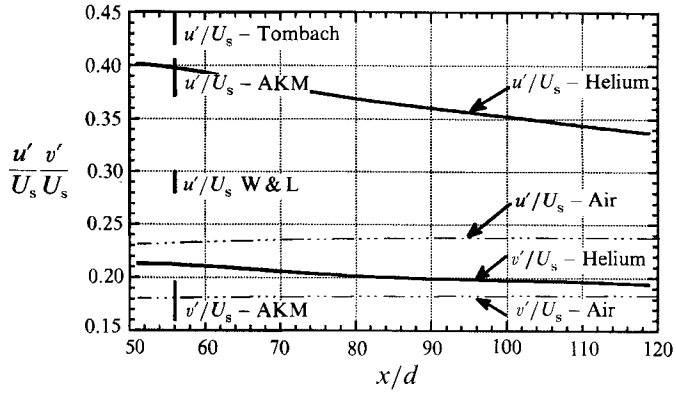

FIGURE 12. Centreline variation of the intensities of axial and radial velocity fluctuations. Vertical bars have been used to indicate the range of values measured by other investigators in helium jets Tombach, x/d = 15–20 as reported in Way & Libby 1970; W & L, Way & Libby 1970 x/d = 15–20; AKM, Aihara *et al.* (1970), x/d = 30–100.

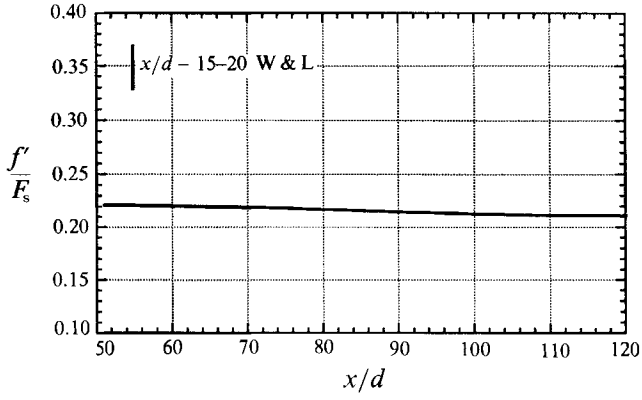

FIGURE 13. Centreline variation of mass fraction intensity.

would be expected from extrapolation of present measurements. Way & Libby's values of 28–30% in the x/d range 15–20 are significantly lower. This x/d range for their flow configuration is very close to the plume region, and as observed by Chen & Rodi, their reported values of u' agree well with measurements in a round plume (see e.g. George *et al.* 1988).

The intensity of helium mass fraction fluctuations as a function of the distance along the axis of the jet is shown in figure 13. It remains essentially constant between 0.21–0.22 and is in agreement with the Chen & Rodi recommendation of 0.21–0.24 for the asymptotic values for flows with density ratio close to unity. Pitts (1986) in his measurements made in jets with co-flow, but designed to emulate free jets, found that the asymptotic value of mass fraction intensity was independent of the density ratio and was about 0.23. This study included a helium jet in co-flow. Pitts' measurements in a free jet of helium were slightly higher, of the order of 0.26. Concurrence of present measurements with those of Pitts indicates that the significantly higher values of Way & Libby (0.33–0.37), which are closer to values reported for plumes (see George *et al.*), may have been caused by buoyancy effects and not by density effects.

The radial profiles of velocity fluctuations are shown in figure 14. The radial

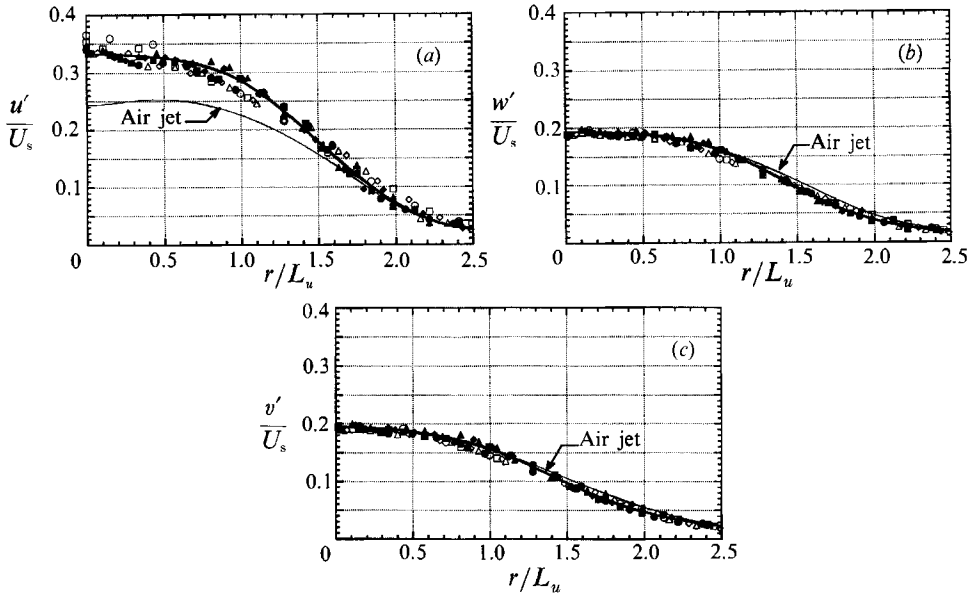

FIGURE 14. Radial variation of intensities of velocity fluctuations. (*a*) Axial intensity, u'/U_s, (*b*) radial intensity v'/U_s, (*c*) azimuthal intensity w'/U_s. See figure 8 for explanation of symbols. 'Air jet' indicates measurements reported in Part 1. The radial distance r has been normalized by L_u, the half-width of the jet.

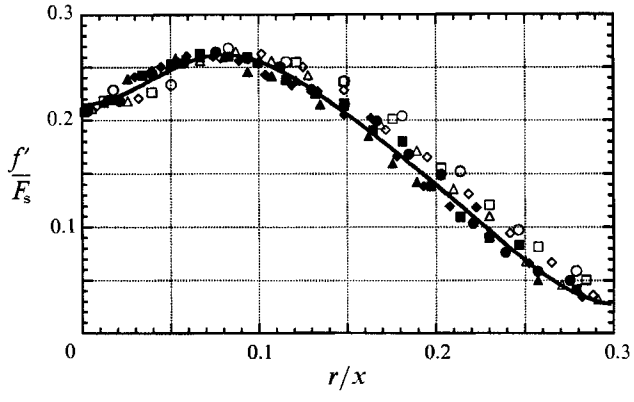

FIGURE 15. Radial variation of concentration fluctuation intensity. See figure 8 for explanation of symbols.

coordinate has been normalized by the half-width of mean velocity: $L_u = 0.116x$ for the helium jet and $L_u = 0.096x$ for the air jet. The profiles for intensities of azimuthal and radial velocity fluctuations in the helium jet are virtually identical with those for the air jet. The intensity of axial velocity fluctuations, as mentioned earlier, is higher than the air jet values in the fully turbulent region near the axis of the jet. In the outer part of the jet where entrainment causes the density to be close to the ambient density the two intensities are not different from each other. There seems to be no significant effect of buoyancy in the outer region.

Variation of mass fraction intensity is shown in figure 15. The distinct off-axis peak and the much wider profile that are characteristic of all scalar fluctuation intensity plots are seen here also. The location of this maximum, $\eta_{\max}$, and the ratio of the maximum to the centreline value, $f'_{\max}/f'_{\mathrm{cl}}$, are two parameters that characterize this

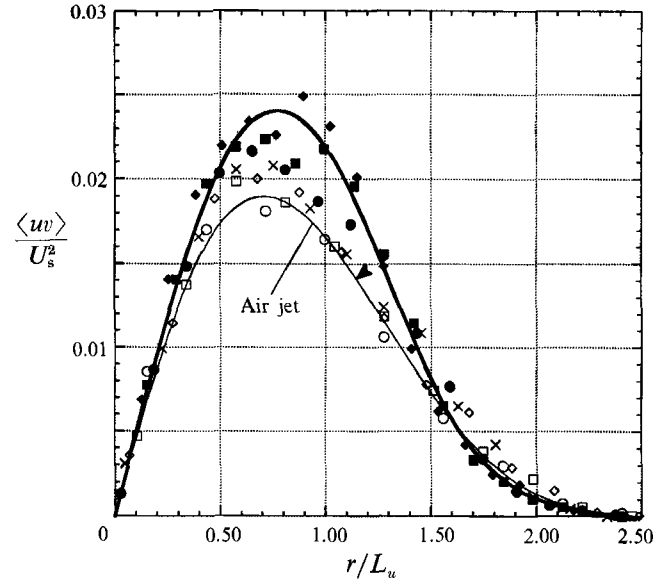

FIGURE 16. Reynolds stress variation across the jet. See figure 8 for explanation of symbols.

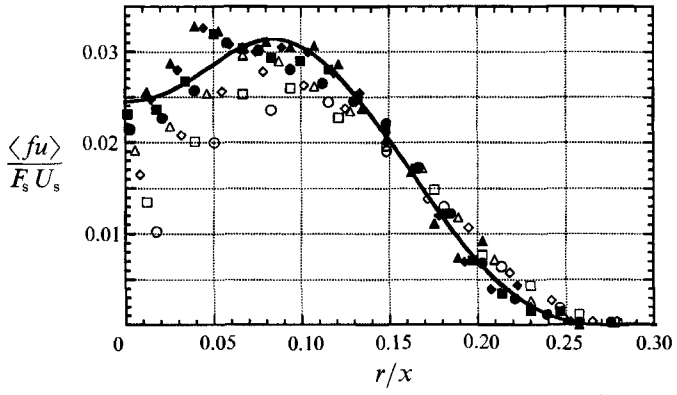

FIGURE 17. Variation of the axial scalar flux $\langle fu \rangle$ across the jet. See figure 8 for explanation of symbols.

variation. For the present measurement $f'_{\max}/f'_{\mathrm{cl}} = 1.27$ and $\eta_{\max} = 0.081$. Gouldin *et al.* (1986) tabulate the values of these two parameters for different investigations of axisymmetric jets with different density ratios. The observed value of the ratio $f'_{\max}/f'_{\mathrm{cl}}$ is in the range of values reported in Gouldin *et al.* of 1.14–1.29. The location $\eta_{\max}$ as a fraction of L_f seems to show a linear trend with the density ratio, described by $\eta_{\max}/L_f = 0.55 + 0.26\,\omega^{-1}$, when considered along with other reported values.

The variation of Reynolds stress across the helium jet is shown in figure 16. The values for the helium jet are higher near the peak than for the air jet, but towards the edge of the jet both agree well with each other. An approximate equation that relates the density difference observed on the centreline to the mean velocity gradient along the axis and the Reynolds stress gradient in the radial direction may be derived from the mean momentum equation. The calculated values and the measured values of the density differences agree well with each other.

The scalar fluxes $\langle fu \rangle$ and $\langle fv \rangle$ are shown in figures 17 and 18. The values of $\langle fu \rangle$ increase with x/d in the central region of the jet in a systematic manner, while

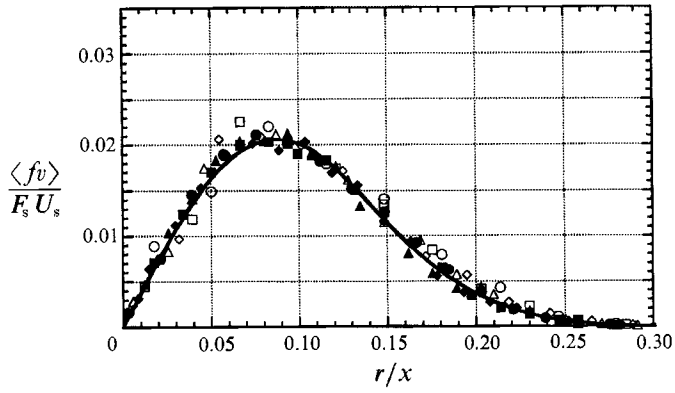

FIGURE 18. Variation of the radial scalar flux $\langle fv \rangle$ across the jet. See figure 8 for explanation of symbols.

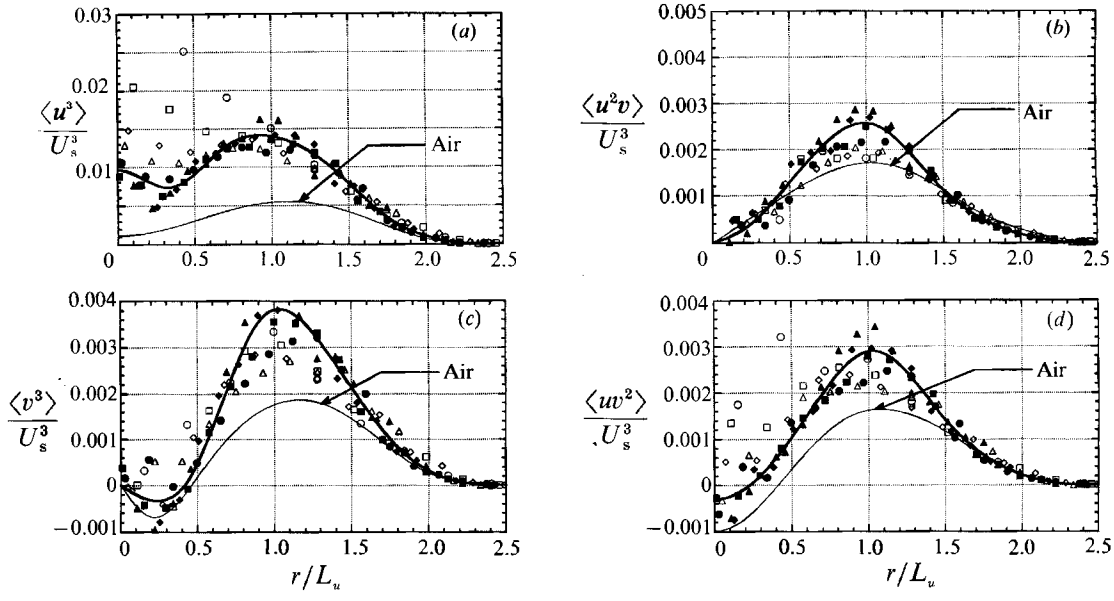

FIGURE 19. Triple moments of velocity fluctuations. (a) $\langle u^3 \rangle$, (b) $\langle v^3 \rangle$, (c) $\langle u^2 v \rangle$, (d) $\langle uv^2 \rangle$. See figure 8 for explanation of symbols.

exhibiting an almost self-similar profile near the edge. The radial flux $\langle fv \rangle$ does not show much deviation from the self-similar profile across the entire jet. The observed values of these two fluxes agree with values reported by Chevray & Tutu from measurements of temperature fluctuations in the near field of the jet ($x/d = 15$).

4.3. *Higher moments*

The triple moments of velocity fluctuations are shown in figure 19. The triple moments involving scalar fluctuations are presented in §4.5 along with model predictions. The levels of velocity triple moments are higher than those observed in the air jet except near the edge of the jet where the air jet values are equal to the helium jet values. The steeper gradients in the triple moments indicate larger

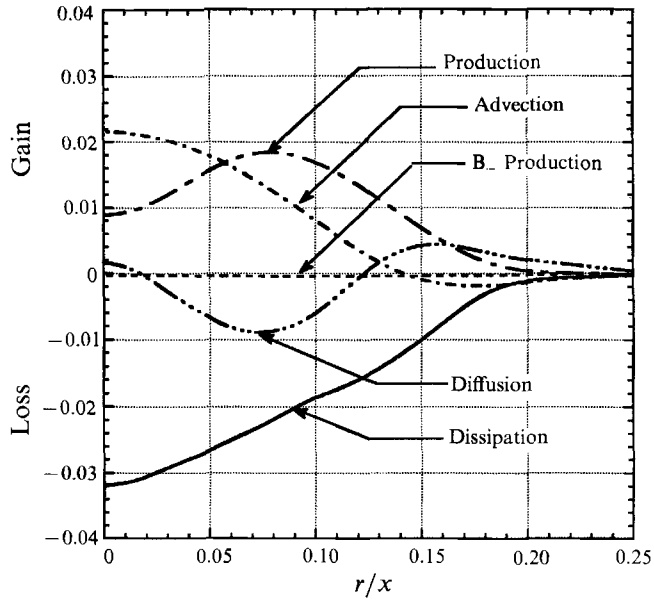

FIGURE 20. Kinetic energy budget for the helium jet based on data in the x/d range 90–120. The term marked B_ Production is an approximate estimate of the buoyant production of kinetic energy at $x/d = 105$.

diffusive fluxes. The negative regions of the triple moments observed in the air jet are observed in the helium jet also. The values of $\langle u^3 \rangle$ indicate a highly skewed distribution of velocity fluctuations in the near field of the jet.

4.4. *Budgets*

The budget for the turbulent kinetic energy is shown in figure 20. The budget follows from the trace of the Reynolds stress equation (10(*a*)). The pressure diffusion term has been neglected in estimating the diffusion term. In variable-density flows pressure diffusion is expected to be more significant than in air jet (see Shih *et al.* 1987), hence there is much less justification for its neglect here. Consequently the term marked 'dissipation' should be regarded as the sum of both dissipation and pressure diffusion, but for the estimation of timescale ratio and for the prediction schemes for triple moments it is taken to represent dissipation.

The structure of the kinetic energy budget is the same as that presented for the air jet in Part 1. In comparison with the budget for the air jet, the levels of all the terms are 1.5 to 2 times higher. This is a consequence of the higher levels of $\langle q^2 \rangle$ which stems from higher levels of $\langle u^2 \rangle$. The turbulent diffusion is higher because of the steeper gradients observed in the third moments in comparison with those for the air jet. The dissipation term does not show the plateau seen in the budget for the air jet, a possible indication that pressure diffusion is substantial in the helium jet.

The term marked B_ 'production' is an approximate estimate of the buoyant production of the turbulent kinetic energy evaluated at the mid-point of the range of x/d considered, i.e. at $x/d = 105$. It can be seen that though buoyancy influences the mean momentum balance significantly at this location it is not felt by the turbulent energy balance. But because of its power-law dependence it will little dominate the budget further downstream as the flow becomes a plume.

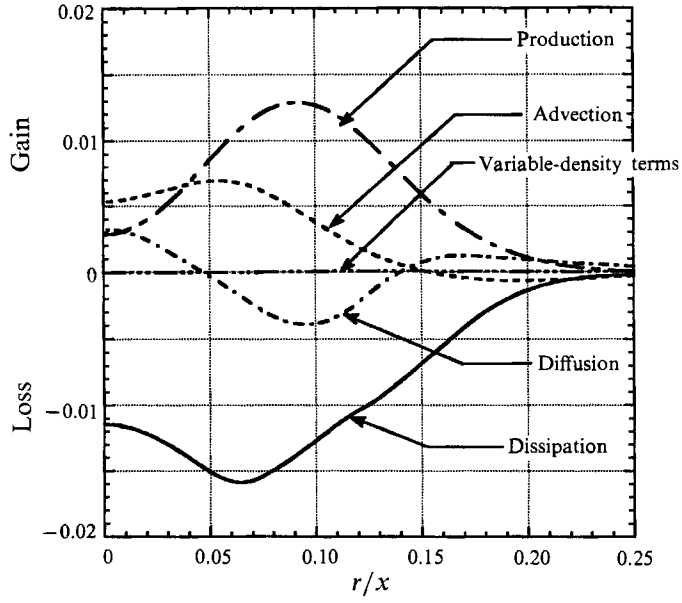

FIGURE 21. Scalar variance budget for the helium jet based on data in the x/d range 90–120.

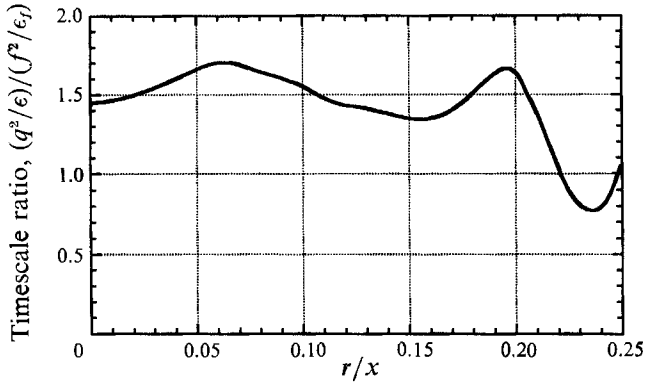

FIGURE 22. The variation of the ratio of mechanical timescale to the scalar timescale derived from the budgets of figures 20 and 21.

The scalar variance budget is presented in figure 21. The relative dominance of the production term is conspicuous. This is brought about by the lower levels of advection due to lower levels of the scalar variance. The distinct off-axis peak follows from this higher level of production. The turbulent diffusion of scalar variance is more pronounced near the axis than the turbulent diffusion of kinetic energy. The structure of the present budget is the same as the one presented by Antonia *et al.* for passive temperature fluctuations in a turbulent round jet in a co-flowing stream, although the levels are different.

The ratio of mechanical to scalar turbulence timescales has been calculated from the dissipation terms of the budgets and the variances. The result is shown in figure 22. The value of the ratio is almost constant at about 1.5 across most of the jet. The variation seen near the outer edge is due to extremely small values of the two timescales.

4.5. *Triple-moment models*

The diffusion terms in the scalar flux equation and the scalar variance equation contain the triple moments $\langle u_i u_j f\rangle$ and $\langle u_i f^2\rangle$. Models need to be provided for these terms to close the equations at the second-moment level. Lumley (1978) describes modelling procedures for these terms. This procedure was considered in Part 1 for the velocity triple moments. Now we consider the models for scalar triple moments. The models for the triple moments are viewed as approximations, i.e. closures, to the triple-moment equations. The order-of-magnitude analysis carried out in Shih *et al.* (1987) indicates that, to first order in density fluctuations, constant-density flow models may be used. The equation for $\langle u_i u_j f\rangle$ in constant-density flows is given by

$$U^m\langle u_i u_j f\rangle_{,m} = P^{(\mathrm{M})}_{ij(f)} + P^{(\mathrm{T})}_{ij(f)} + d_{ij(f)} + \phi_{ij(f)} - \epsilon_{ij(f)}, \tag{18}$$

where

$$\begin{aligned}
P^{(\mathrm{T})}_{ij(f)} &= [\langle u_j f\rangle\langle u^m u_i\rangle_{,m} + \langle f u_i\rangle\langle u^m u_j\rangle_{,m} + \langle u_i u_j\rangle\langle u^m f\rangle_{,m}],\\
P^{(\mathrm{M})}_{ij(f)} &= -[\langle u_j f u^m\rangle U_{i,m} + \langle f u_i u^m\rangle U_{j,m} + \langle u_i u_j u^m\rangle F_{,m}],\\
d_{ij(f)} &= -[\langle u_i u_j f u^m\rangle - g^k_m[(\gamma+\nu)\langle u_i u_j f\rangle_{,k} + \nu\langle u_i u_j f_{,k}\rangle\\
&\quad + \gamma\langle f u_i u_{j,k}\rangle + \gamma\langle f u_j u_{i,k}\rangle]_{,m},\\
\phi_{ij(f)} &= (1/\rho)[\langle p_{,i}(u_j f)\rangle + \langle p_{,j}(f u_i)\rangle],\\
\epsilon_{ij(f)} &= (\gamma+\nu) g^k_m[(\langle u_i u_{j,k} f_{,m}\rangle + \langle u_{i,k} u_j f_{,m}\rangle) + 2\nu\langle f u_{i,m} u_{j,k}\rangle].
\end{aligned}$$

The equation for $\langle u_i f^2\rangle$ is similar, which we indicate briefly as

$$U^m\langle u_i f^2\rangle_{,m} = P^{(\mathrm{M})}_{i(ff)} + P^{(\mathrm{T})}_{i(ff)} + d_{i(ff)} + \phi_{i(ff)} - \epsilon_{i(ff)}. \tag{19}$$

We will drop the subscripts for brevity from now on. $P^{(\mathrm{T})}$ and $P^{(\mathrm{M})}$ are production by the turbulent and mean fields respectively and are 'closed' terms. The molecular terms in the diffusion terms, d, are neglected in comparison with the turbulent contribution. Measured fourth moments indicate that the quasi-Gaussian approximations to the diffusion terms are very good across the entire jet including the intermittent region. Measurements indicate that the advection terms on the left-hand side are negligible. The pressure terms ϕ and the dissipation terms ϵ need to be modelled. As indicated in Part 1 the models for the pressure terms are divided into two parts: $\phi^{(1)}$ – the rapid part, and $\phi^{(2)}$ – the return-to-isotropy part. We consider two models for the triple moments, *Basic* and *Full*, which approximate the triple-moment equation with the following equations:

$$\textit{Basic}: \quad P^{(\mathrm{T})} + d + \phi^{(2)} + \epsilon = 0, \tag{20}$$

$$\textit{Full}: \quad P^{(\mathrm{M})} + P^{(\mathrm{T})} + d + \phi^{(1)} + \phi^{(2)} + \epsilon = 0. \tag{21}$$

The specific models for the unclosed terms in the above equations are described in detail in Lumley (1978) and Shih *et al.* (1987). We now give the explicit representation for the triple moments that follow from the *Basic* models:

$$\langle u_j f^2\rangle = -[\langle f^2\rangle_{,m}\langle u_j u^m\rangle + 2\langle u_j f\rangle_{,m}\langle u^m f\rangle]\langle q^2\rangle/2\epsilon(r+\phi^f), \tag{23}$$

$$\begin{aligned}
\langle u_i u_j f\rangle = (&-[u_i f\rangle_{,m}\langle u^m u_j\rangle + \langle u_j f\rangle_{,m}\langle u^m u_j\rangle + \langle u_i u_j\rangle_{,m}\langle u^m f\rangle]\\
&+ \frac{\beta-2}{3}\frac{\langle\epsilon\rangle}{\langle q^2\rangle}\langle q^2 f\rangle g_{ij})\frac{\langle q^2\rangle}{\langle\epsilon\rangle(\beta+2\Phi^f)},
\end{aligned} \tag{24}$$

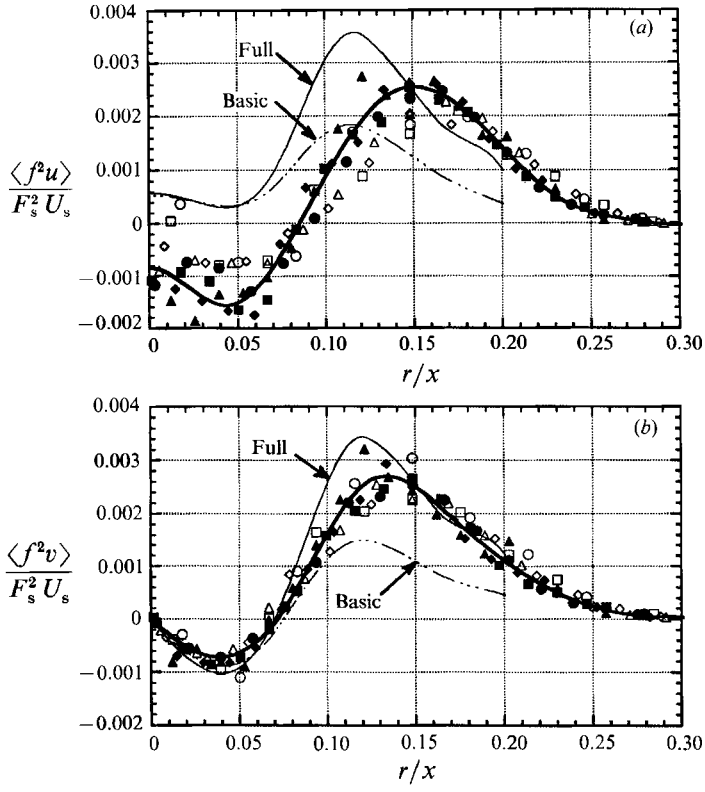

FIGURE 23. Plot of triple moments (*a*) $\langle f^2u\rangle$ and (*b*) $\langle f^2v\rangle$ and comparisons with *Basic* and *Full* models described in §4.5.

where r is the ratio of timescales and Φ^f is given by

$$\Phi^f = \frac{\beta}{2} + r - \frac{(\beta-2)Q}{2(P+Q)} + 1.1r^2F_D^{\frac{1}{2}}$$

$$Q = \tfrac{1}{6}(1-D_i^i 2), \quad P = (D_j^i b_k^j D_i^k - b_i^j D_j^i),$$

$$F_D = (9D_i^{i2} - \tfrac{27}{2}D_i^{i3} + \tfrac{9}{2}),$$

$$D_j^i = \frac{\langle f^2\rangle\langle u^i u_j\rangle - \langle u^i f\rangle\langle u_j f\rangle}{\langle f^2\rangle\langle q^2\rangle - \langle u_m f\rangle\langle u^m f\rangle}. \tag{25}$$

The return-to isotropy coefficient β is as defined in Part 1. Simple linear models are used for the rapid pressure terms similar to the one used for the velocity triple moments. Together with the mean field production terms they result in the following expressions:

for $\langle u_j f^2\rangle$: $\phi^{(2)} + P^{(M)} = \langle u_i u^m f\rangle F_{,m} + \frac{2}{5}\langle u^m f^2\rangle S_{im}$, (26*a*)

for $\langle u_i u_j f\rangle$: $\phi^{(2)} + P^{(M)} = \langle u_i u_j u^m\rangle F_{,m} + \frac{2}{5}(\langle u_j u^m f\rangle S_{im} + \langle u_i u^m f\rangle S_{jm})$. (26*b*)

The addition of these terms to the *Basic* model gives the *Full* model which is a set of coupled linear algebraic equations for the triple moments. These two models have been calculated for the present flow using measured values of second moments and the dissipation terms estimated from the budgets. In the *Full* model for $\langle u_i u_j f\rangle$

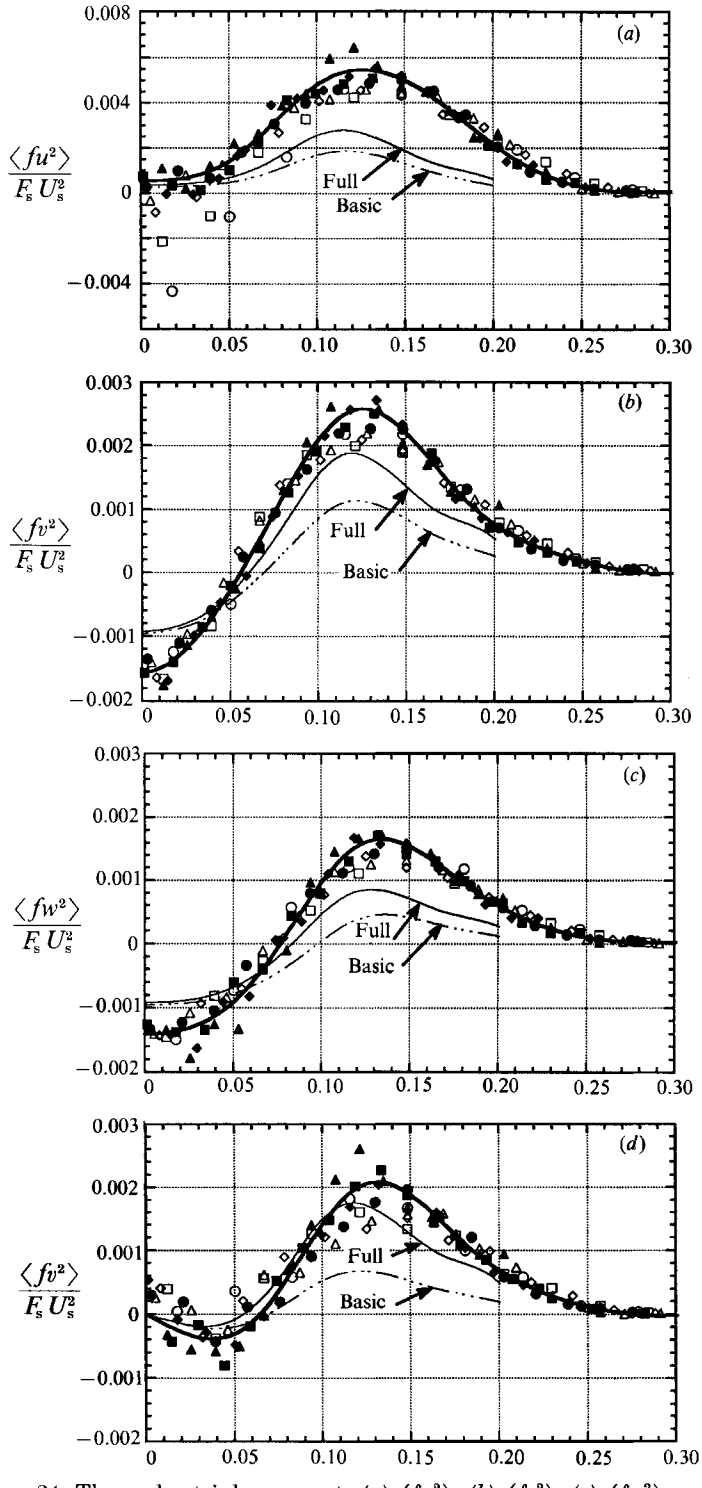

FIGURE 24. The scalar triple moments (*a*) $\langle fu^2 \rangle$, (*b*) $\langle fv^2 \rangle$, (*c*) $\langle fw^2 \rangle$ and (*d*) $\langle fuv \rangle$ and comparisons with *Basic* and *Full* models described in §4.5.

experimental values of velocity triple moments have been used, and similarly for $\langle u_i u^m f \rangle$ in the model for $\langle u_j f^2 \rangle$. The assumption of self-similarity has been used as described in Part 1 to calculate the derivatives. This, as indicated earlier, is only approximately valid for the present flow.

The results of the calculations along with measurements are shown in figures 23 and 24. The performance of the more elaborate *Full* model is very satisfactory in the full turbulent zone, $\eta < 0.12$, except for correlations involving axial velocity fluctuations. The *Basic* model is inferior to the *Full* model in describing all the triple moments. Neither model does well in the intermittent region. The reason for this, as indicated in Part 1, must lie with the models for the pressure and dissipation terms and not with the quasi-Gaussian description of the diffusion term. The performance of the full models for the velocity triple moments, which we have not presented here, was similar to that observed for the air jet. Based on similar performance of the models in air jets and helium jets we conclude that constant-density flow models are adequate for triple moments with small density fluctuations in the fully turbulent zone.

5. Conclusions

Comprehensive turbulence measurements of both velocity and helium concentration fields in a helium jet have been presented. The mass flux of helium across the jet, considering only the mean field contribution, is within $\pm 10\%$ of the nozzle input. The measurements reported here lie in the intermediate region between the non-buoyant jet region and the plume region.

The mean velocity decay along the axis agrees with the scaling indicated by the effective diameter. The mean concentration field decay, which agrees with earlier measurements, indicates a density ratio dependence that is different from that suggested by the effective diameter. Both velocity and concentration fields are seen to approach the scaling for the plume in the far field. The radial profile of mean velocity is wider than that for the air jet, a consequence of the mean momentum added by the buoyancy. The spreading rates of the mean velocity and concentration fields indicate a turbulent Schmidt number of 0.7, which agrees with other measurements of scalars in round jets.

Significantly higher levels of axial velocity turbulent intensities are observed. This has also been observed by other investigators. It is believed that the origins of these higher levels must lie in the near-field development of the jet, a region not studied in the present investigation. Moments that involve axial velocity fluctuations do not seem to approach a self-similar behaviour, while those that do not contain axial velocity fluctuations seem to do so.

Current models for scalar triple moments were evaluated. The model termed the *Full* model, that neglects only the advection term in the triple-moment equation and models all other unknown terms, is found to be satisfactory in the fully turbulent region but inadequate in the intermittent region. The same conclusion was reached based on the velocity triple moments in Part 1. This indicates that the practice of using simpler models for turbulent diffusion that neglect the effects of mean fields needs to be examined.

REFERENCES

AIHARA, Y., KOYAMA, H. & MORISHITA, E. 1974 Effects of an air stream on turbulent diffusion of helium jet from a small nozzle. *Phys. Fluids* **17**, 665–673.

CHEN, C. J. & RODI, W. 1980 *Vertical Turbulent Buoyant Jets – A review of Experimental Data.* HMT-4. Pergamon.

CORRSIN, S. 1949 Extended applications of the hot-wire anomometer. *NACA Tech. Note* 1864.

GEORGE, W. K., CAPP., S. P., SEIF, A. A.,BAKER, C. B. & TAULBEE, D. B. 1988 A study of the turbulent axisymmetric jet. *J. Engng Sci. King Saud Univ.* **14**, 85–93.

GOULDIN, F. C., SCHEFFER, R. W., JOHNSON, S. C. & KOLLMAN, W. 1986 *Prog. Energy Combust. Sci.* **12**, 257–303.

KEAGY, W. R. & WELLER, A. E. 1949 A study of freely expanding inhomogeneous jets. *Heat Transfer Fluid Mech Inst.* **x**, 89–98.

LUEPTOW, R. M., BREUER, K. S. & HARITONIDIS, J. H. 1988 Computer-aided calibration of ×-probes using a look-up table. *Exp. Fluids* **6**, 115–118.

LUMLEY, J. L. 1978 Computational modelling of turbulent flows. *Adv. Appl. Mech.* **18**, 123–176.

OGINO, F., TAKEUCHI, H., KUDO, I. & MIZUSHINA, T. 1980 Heated jet discharged vertically into ambients of uniform and linear temperature profiles. *Intl J. Heat Mass Transfer* **23**, 1581–1588.

PANCHAPAKESAN, N. R. & LUMLEY, J. L. 1993 Turbulence measurements in axisymmetric jets of air and helium. Part 1. Air jet. *J. Fluid Mech.* **246**, 197–223.

PAPANICOLAOU, P. N. & LIST, E. J. 1987 Statistical and spectral properties of tracer concentration in round buoyant jets. *Intl J. Heat Mass Transfer* **30**, 2059–2071.

PITTS, W. M. 1986 Effects of global density and Reynolds number variations on mixing in turbulent, axisymmetric jets. *NBSIR* 86-3340. National Bureau of Standards, US Department of Commerce.

RODI, W. 1982 *Turbulent Buoyant Jets and Plumes.* HMT-6. Pergamon.

SHIH, T.-H., LUMLEY, J. L. & JANICKA, J. 1987 Second-order modelling of a variable-density mixing layer. *J. Fluid Mech.* **180**, 93–116.

SIRIVAT, A. & WARHAFT, Z. 1982 The mixing of passive helium and temperature fluctuations in grid turbulence. *J. Fluid Mech.* **120**, 475–504.

THRING, M. W. & NEWBY, M. P. 1953 Combustion length of enclosed turbulent jet flames. *Fourth (Intl) Symp. Combustion*, pp. 789–796. The Williams & Wilkins Co., Baltimore, MD.

WAY, J. & LIBBY, P. A. 1970 Hot-wire probes for measuring velocity and concentration in helium and air mixtures. *AIAA J.* **8**, 976–978.

WAY, J. & LIBBY, P. A. 1971 Application of hot-wire anemometry and digital techniques to measurements in a turbulent helium jet. *AIAA J.* **9**, 1567–1573.